A lithium-ion battery based on LiFePO$_4$ and silicon/reduced graphene oxide nanocomposite

Pier Paolo Prosini [a,b,*], Maria Carewska [a], Fabio Maroni [c], Roberto Tossici [c], Francesco Nobili [c]

[a] ENEA, Italian National Agency for New Technologies, Energy and Sustainable Economic Development, Casaccia Research Centre, Via Anguillarese 301, 00123 Santa Maria di Galeria, Rome, Italy
[b] DInESto, Drive the Innovation in Energy Storage, Via Province, 04012 Cisterna di Latina, Italy
[c] Chemistry Division, School of Science and Technology, University of Camerino, Via S. Agostino, 62032 Camerino (MC), Italy

ARTICLE INFO

ABSTRACT

In this paper, the preparation and chemical–physical characterization of a composite material made of silicon nanoparticles (nSi) and reduced graphene oxide (RGO) for using as an anode for lithium-ion batteries are reported. The nSi/RGO composite was synthesized by microwave irradiation followed by a thermal treatment under reducing atmosphere of a mixture of nSi and graphene oxide, and characterized by XRD, SEM, and TGA. The nanostructured material was used to prepare an electrode, and its electrochemical performance was evaluated in a lithium cell by galvanostatic cycles at various charge rates. The electrode was then coupled with a LiFePO$_4$ cathode to fabricate a full lithium-ion battery cell and the cell performance evaluated as a function of the discharge rate and cycle number.

1. Introduction

Lithium-ion batteries (LIBs) represent one of the most important mobile power sources for laptops, cameras, and smart phones. However, the current energy density of LIBs is approaching its theoretical limit [1], underscoring the urgent need for new high energy density battery systems. To increase the energy density, new electrode materials characterized by higher specific capacity or higher voltage should be developed. At present, the most promising electrode materials to enhance the energy density of LIBs are silicon-based composites for the anode and high voltage metal oxides for the cathode. Silicon is the most promising candidate to replace conventional carbon-based anodes in LIBs, because it offers a large practical capacity (up to 3600 mAh/g) [2], and an electrochemical alloy/de-alloy reaction voltage of below 0.5 V (vs. Li/Li$^+$) [3]. However, its practical application has been hindered by the huge volume change [4] (up to 300%) during the repeated charge/discharge process. The volume variations cause particle pulverization and consequently contact loss between the particles which has been believed to be at the origin of the capacity fade that affects this material. A number of strategies have been implemented to contain the volume change and enhance or maintain the electric contact between silicon and the conductive agent. Examples include silicon nanowires [5], silicon nanotubes [6], porous silicon [7], and Si dispersed in a carbon matrix [8,9]. This last approach consists into preparing composites with nano-Si particles/clusters dispersed uniformly in a carbonaceous matrix. The matrix is able to buffer the large volume expansion and enhance Si conductivity during cycling [10–13]. Different kinds of carbonaceous materials combined with nano-Si, such as graphite [9,14-15], pyrolyzed carbon [16], mesoporous carbon [17], and carbon nanotubes [18] have been investigated. Recently, it has been observed that graphene can be advantageously used as an active/inactive matrix [19]. It has been stated that nanosize silicon/graphene composite can accommodate the large strains of lithium insertion and de-insertion and provide good electrical contact owing to the good mechanical properties and high conductivity provided by graphene. Starting from this work, a large number of papers dealing with nanosize silicon/graphene composite have been published. Graphene could serve not only as an inactive confining buffer to accommodate the large volume change of Si during LIB cycling, but also as a highly conductive agent [20–33]. Despite the numerous reports on Si–graphene anode materials, most of the data come from tests performed on half cells and only few papers report on the behavior of full lithium-ion cells [34–36]. To demonstrate the feasibility of the silicon-based anode, Ji et al. [34] assembled a full lithium-ion cell composed of graphene/Si multilayer structure as an anode and commercially available LiNi$_{1/3}$Mn$_{1/3}$Co$_{1/3}$O$_2$ as a cathode. Initial results showed good electrochemical performance comparable to that of commercially available rechargeable LIBs. Ren et al. prepared a 3.6 V full-cell device by combining a Si–graphene anode with a Li-excess layer-structured composite Li$_{1.2}$Ni$_{0.2}$Mn$_{0.6}$O$_2$ cathode [35]. These full-cell studies did not report

the active material ratio for the electrodes. The lower performance might be due to the limited supply of cyclable lithium provided by the positive electrode, an increase in resistance of components by additional SEI formation, or dissolution of electrolyte and metals from the cathode. To better understand the cause for the greater capacity fade in full cells Eom et al. designed a full lithium-ion cell employing a nano-Si–graphene composite anode with a NCA cathode and investigated its electrochemical and microstructural behaviors during charge/discharge cycling [36]. They showed that the principal problems related to the cycling of a full lithium-ion cell with a Si–graphene anode are related to the large initial irreversible capacity loss of the anode and to the continuous SEI formation during cycling. In this work, we tested a nano-silicon/reduced graphene oxide (nSi/RGO) composite in a full lithium-ion cell coupling this electrode with a LiFePO$_4$-based cathode. To exploit the reversible capacity of the nSi/RGO anode avoiding the very high irreversible capacity loss needed for activation of the fresh electrode and the loss of capacity observed in the following cycles, we first cycled a nSi/RGO anode in a lithium cell and then used the cycled electrode in a full lithium-ion cell. For this purpose, the nSi/RGO was first electrochemical characterized in a lithium metal half-cell and then coupled with a commercial LiFePO$_4$ cathode to fabricate a full lithium-ion battery cell. The so obtained cell was electrochemically characterized in terms of capacity retention as a function of the discharge rate and cycle number.

2. Experimental

2.1. Synthesis of nSi/RGO

The preparation of nSi/RGO is reported in a previous published work [37]. Briefly, the commercial powder of graphene oxide (GO) (Nanoinnova®) was dispersed in ethylene glycol by ultrasonication for 2 hours. Low molecular weight polyacrylic acid (PAA, Mw = 2000) was added in a GO:PAA ratio of 1:4 (w/w), and dispersed through ultrasonication for 1 hour in order to allow GO functionalization by PAA. Crystalline silicon nanoparticles prepared by laser-driven aerosol synthesis from vapor phase (Alfa–Aesar) with an average particle size less than 50 nm and a purity of 98% were used. The powder of Si nanoparticles was added to the GO in a molar ratio GO:Si of 5:1 and the suspension was sonicated for additional 2 hours. The so obtained suspension was subjected to a first reduction step by microwave heating conducted for 20 minutes at 540 W. After the microwave treatment the powder was vacuum filtered on a hydrophobic filter (Fluoropore®), washed with ethanol and dried in an oven at 50 °C. A second thermal reduction step was conducted by heating the powder at 700 °C in 95:5 Ar/H$_2$ atmosphere for 8 hours.

2.2. Chemical–physical characterization of nSi/RGO

High magnification microphotographs were obtained by using an AURIGA, CrossBeam Workstation dual column Focused Ion Beam–SEM. The structures of the materials were characterized by X-ray powder diffraction analysis (Rigaku Miniflex) using Cu–Kα radiation. Thermal stabilities were verified in nitrogen using a simultaneous TG-DTA (Q600 SDT, TA Instruments) equipped with the Thermal Solution Software (version 1.4). The temperature was calibrated using the nickel Curie point as the reference. The mass was calibrated using ceramic standards provided with the instrument. High purity aluminium oxide was used as the reference material. Open platinum crucibles (cross-section = 0.32 cm^2) were used to contain the samples. The experiments were performed on 10–12 mg samples that were stored, handled, and weighed in a dry room. The thermal stability was investigated by heating the samples from room temperature up to 750 °C at a rate of 10 °C min^{-1}. The onset temperature was calculated by thermal analysis software (Universal Analysis version 2.5) as the intersection between

the extrapolated baseline weight and the tangent through the inflection point of the weight vs. temperature curve.

2.3. Preparation of the composite anodes

0.106 g of the active material (nSi/RGO) and 0.040 g of carbon (SuperP) were weighed and mixed in a mortar for 5 minutes 0.015 g of the binder (Teflon PTFE 6C, DuPont) was weighed and added to the mixture. The blend was intimately mixed to obtain a plastic-like material. Composite electrode tapes were made by roll milling the plastic-like material. The quantities of active material, binder, and carbon in the tape were 65 wt.% nSi/RGO, 10 wt.% Teflon, and 25 wt.% SuperP. The specific weight of the tape was 4.6 mg/cm^2, resulting in an active material loading (nSi/RGO) of 3 mg/cm^2.

2.4. Preparation of the composite cathode

1.5 g of lithium iron phosphate (Gelon lib Group, ShanDong, P.R. China) and 0.25 g of carbon black (Super P, MMM Carbon) were weighed and transferred to a mechanic mill (Mixer Mill MM200, Retsch). The mixture was mixed by operating the device for a few minutes. 0.5 g of poly(vinyl acetate) (PVAc) with a solid mass fraction of 50% (Vinavil SpA via Valtellina, 63 – 20159 Milano – Italia) was diluted with 5 ml of water. The solution of PVAc was added to the powder mixture and the components were mixed by operating the mill for a few minutes. The so obtained suspension was used to paint a thin aluminum sheet covering a surface area of 100 cm^2. A brush with flat tip of approximately 1 cm width was used to paint the current collector being careful of depositing a uniform layer of suspension on the whole surface of the electrode. After drying in air at 130–150 °C, the procedure was repeated as many times as was necessary to use up the entire suspension. A typical positive electrode composition was 75 wt.% LiFePO$_4$, 12.5 wt.% PVAc, and 12.5 wt.% SuperP. The specific weight of the tape was 20.0 mg/cm^2. Prior to the electrochemical characterization, the electrode was dried by heating under vacuum at 110 °C.

2.5. Electrochemical characterization

For the electrochemical characterization, circular electrodes with a diameter of 12 mm (surface area = 1.13 cm^2, nSI/RGO amount estimated as ~3.4 mg) were punched from the anode tape. The electrochemical properties of the electrodes were tested in a two-electrode lithium cell in which lithium acted both as counter and reference electrode. Lithium-ion batteries were assembled by sandwiching a glass fiber, used as the separator, between the positive and the negative electrode. The cycling performance and cycle life of the cells were evaluated in 2032-type coin cells. Coin cells were filled with a 1.0 M solution of LiPF$_6$ dissolved in ethylene carbonate/diethyl carbonate (1:1). The cycling tests were automatically carried out with a battery cycler (Maccor 4000). Material handling, composite cathode preparation, cell assembly, test and storage were performed at 20 °C in a dry room (R.H. <0.1% at 20 °C).

3. Results and discussion

3.1. Chemical–physical characterization of the nSi/RGO

The nSi/RGO material is presented as a light brown-colored powder. X-ray diffraction (XRD) measurements were employed to investigate the phase and structure of the synthesized samples and Fig. 1 shows the relative diffractogram. All the peaks belonging to crystalline silicon, as reported in the Joint Committee on Powder Diffraction Standards (JCPDS) No. 27-1402, are present in the diffractogram (marked as *). In addition to the peaks belonging to silicon, other three peaks, located at $2\theta = 11.1°$, $18.1°$, and $26.1°$ are visible in the diffractogram. As regards the latter, broad peak centered at about $2\theta = 26.1°$, it typically describes
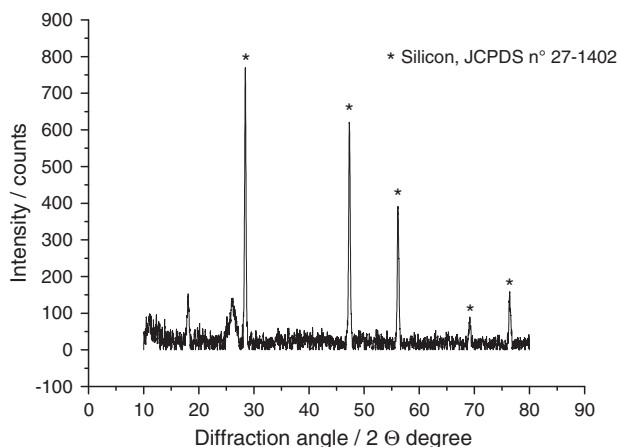
Fig. 1. XRD pattern of the material prepared by heating the precursor at 800 °C under reducing atmosphere. The asterisked peaks are those belonging to crystalline silicon (JCPDS no 27–1402).

the formation of an RGO structure [37,38], which tends to partially re-stack during the high-temperature treatment (graphene nanosheets). The peaks at $2\theta = 11.1°$ and $18.1°$ may be attributed to some residual GO [39] and PAA-functionalized GO [37], suggesting that the final product may contain minor impurities coming from incomplete reduction. It should be emphasized that the reduction conditions were not optimized and that the product purity could be improved by varying the time and the reaction temperature. The silicon is present with a diamond structure belonging to the space group Fd-3 m. The peaks are broadened enough to confirm the presence of a structure with nanometer-sized particles. The particle size was determined by applying the Scherrer's equation to the three main Si peaks located at $2\theta = 28.4°$, $47.3°$, and $56.1°$. The crystallite size ranges between 28.4 and 55.8 nm, as a function of the considered peak. We have also observed that the crystallite size is not changed as a result of the synthesis process.

The morphology of the material is investigated by scanning electron microscopy. Fig. 2 shows a high magnification image of the nSi/RGO. It is possible to distinguish two main morphological structures: the first is a layered structure resulting from the aggregation of some few-nanometer thick overlapped sheets, while the second is formed by branched aggregates composed of spherical particles. Obviously, the first structure can be related to the partly restacked RGO nanosheets, while the second one is associated with aggregates of silicon. From the image, we can see that many Si nanoparticles seem to simply aggregate one to each other while others are efficiently wrapped by the RGO
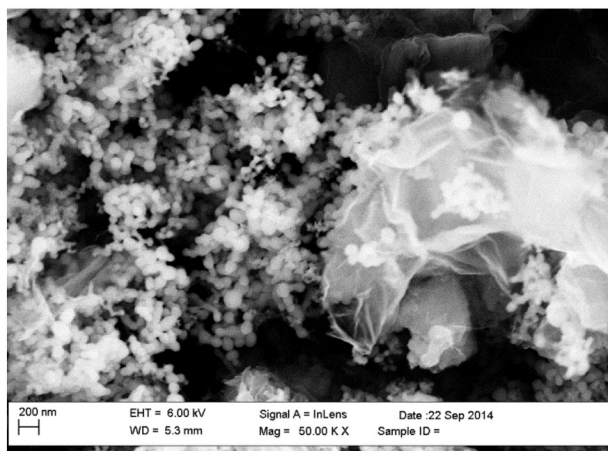

Fig. 2. Scanning electron micrographs of the nSi/RGO nanocomposite.

nanosheets, revealing that at least a portion of the active Si can potentially benefit from the buffering action of RGO matrix. Most of the Si nanoparticles have a diameter of around 50 nm while it is also possible to observe particles with a greater diameter. In any case, the diameter of the largest particles is less than 200 nm. Except for a single-crystal nanoparticle in which crystallite size and particle size are identical, the crystallite size is generally lower than the particle size. This is due to the presence of polycrystalline aggregates that increase the particle size. On the other hand, as the crystallite size approaches the particle size, we have single-crystal nanoparticles. In our case, the grain size of the samples estimated from the SEM picture is larger than that obtained from XRD data. This means that the SEM picture indicates the size of polycrystalline particles formed by aggregation of several crystallites.

The thermal property of the nSi/RGO and the percentage of silicon and carbon in the composite were evaluated by TG analysis, which was performed in air atmosphere with a heating rate of 10 °C/min in the range 20–750 °C. TGA measurement provides further proofs of the reduction of graphene oxide by the thermal treatment. In fact, as shown in Fig. 3, with the increasing of the temperature, the nSi/RGO shows no weight variations up to 450 °C, confirming a good thermal stability due to the absence of labile oxygen functional groups on the RGO. A small weight loss occurs between 420 °C and 550 °C, which can be assigned to the oxidation of graphene present on the surface of the nSi/RGO composite. After that, an abrupt weight loss occurs between 550 °C and 650 °C, which can be assigned to the oxidation of graphene present on the bulk of the nSi/RGO composite. Correspondingly, the DSC curve shows a strong exothermal peak centered at 630 °C. With further heating, little weight loss occurs until 750 °C. The weight percentage of the final remainder was about 31.2 wt. %, revealing the contents of Si in the composite. Since the process of thermal oxidation of the silicon in the temperature range examined is very slow [40], in this determination was not taken into account the weight of any layer of silicon oxide formed on the surface of the grains. By combining this result with the electrode composition described in Par. 2.3, a Si loading in the electrodes can be estimated as about 0.9 ~ 1 mg/cm².

3.2. Electrochemical characterization of the nSi/RGO electrode

Fig. 4a shows the voltage profiles of some relevant initial cycles for the nSi/RGO electrode, cycled galvanostatically with a current of 0.05 mA between 0.01 V and 2.5 V. The applied current corresponds to specific currents, calculated with respect to the weights of nSi/RGO and Si, of about 15 and 48 mA/g, respectively. The open circuit potential (OCV) of the electrode is approximately 2.5 V vs. Li$^+$/Li. Upon lithiation, the voltage quickly decreases below 0.8 V. For further lithium insertion, the voltage slowly declines allowing the insertion of a large amount of lithium and evidencing a large plateau in a potential window approximately between 0.75 V and 0.4 V. After that, the potential decreases with a higher slope until a new plateau, below 0.15 V, is evidenced. In charge, the cell voltage quickly increases to about 0.2 V. Lithium extraction is then revealed by two pronounced shoulders below 1.0 V, while a monotonous sloping line describes further electrode charge up to 2.5 V. The capacity associated with the first discharge is about 3.7 mAh, while the one associated with the subsequent charge is about 1.1 mAh, resulting in a very large first-cycle irreversible capacity loss (ICL) and in a Coulombic efficiency of about 30% (Fig. 4b). After the first cycle, quite reproducible profiles upon both discharge and charge are evidenced. The discharge capacity progressively decreases from 1.68 to 1.35 mAh, while the charge capacity shows an opposite trend increasing from 1.18 to 1.35 mAh, probably because of the progressive 'activation' (i.e. wetting by electrolyte) of larger portions of electrode material upon cycling. As a consequence, after 6 cycles the capacities in charge and discharge converge and the Coulombic efficiency approaches unity.

There are two possible ways to explain the origin of the high capacity loss observed during the first lithiation cycle. From a point of view,
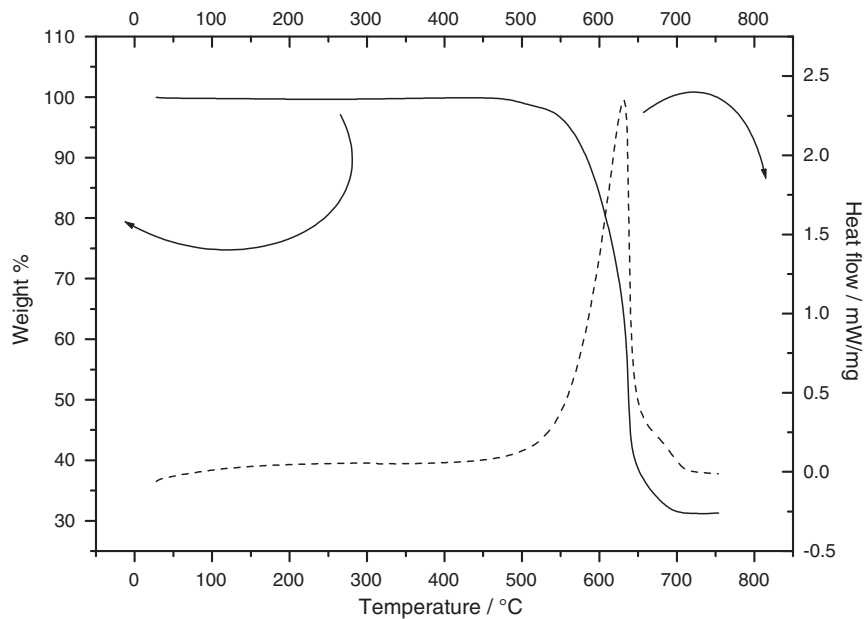
Fig. 3. Termogravimetry (solid line) and differential scanning calorimetry (dash line) for the nSi/RGO nanocomposite conducted from room temperature up to 750 °C at a rate of 10 °C/min under air.

the irreversible capacity could be attributed to a decomposition process involving molecules of the solvent and the electrolyte in contact with the surface of the RGO. On the other hand, it is also possible that lithium is inserted into silicon during the first discharge but then lithium is made unavailable in the next charge cycle. This can be due to the fact that silicon loses his connection with the conductive substrate or because the lithium segregates inside the silicon particle. The very large

first-cycle ICL, and the reversible charge/discharge behavior of the electrode, can be explained by analyzing the calculated dQ/dE vs. V differential profiles shown in Fig. 4c. The differential profile of the first discharge shows a large amount of capacity exchanged by irreversible processes in the voltage range 0.8–0.2 V. This can be mainly ascribed to the formation of a solid electrolyte interphase (SEI) between the electrolyte and the active material, taking place preferentially at the surface of RGO
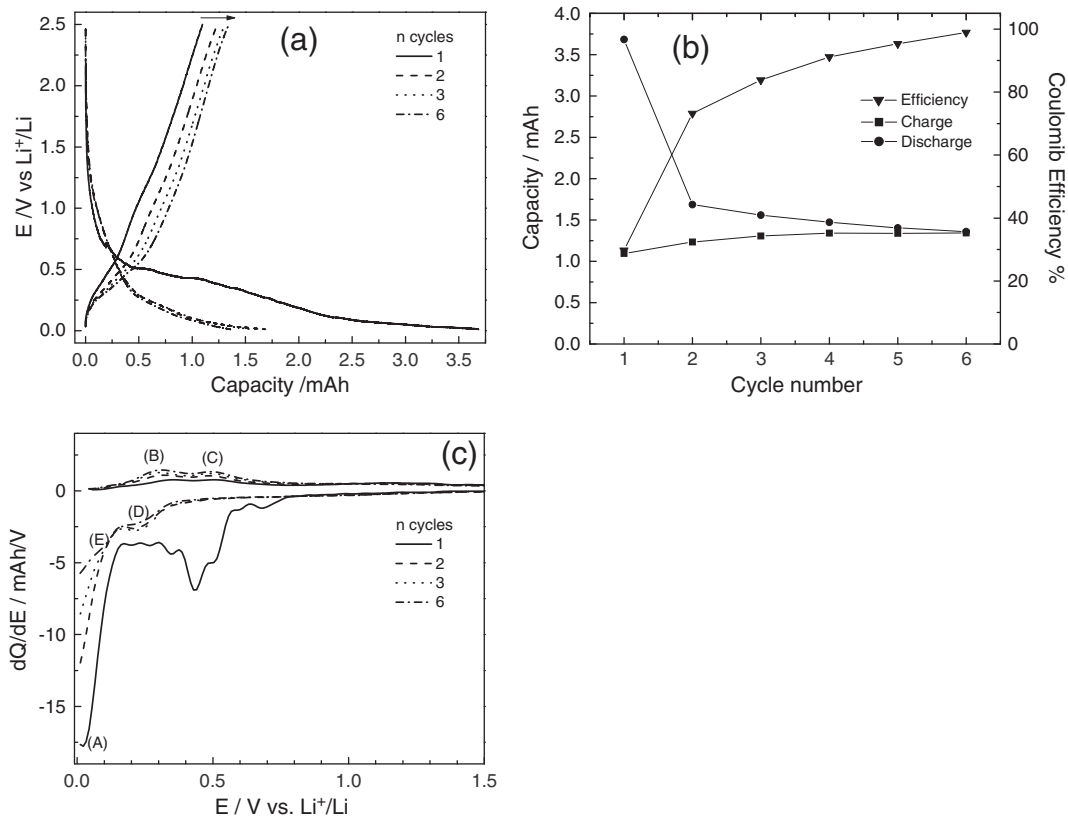

Fig. 4. (a) Voltage profiles for a cell containing the nSi/RGO and cycled at 0.05 mA. (b) Capacity in charge and discharge (left axis) and efficiency (right axis) for the previous described cell. (c) Differential dQ/dE vs. E profiles corresponding to the voltage profiles shown in panel (a).

nanosheets. This is the main reason for the very large ICL, which is commonly [37,41–43] evidenced for composite materials where an amorphous carbon matrix is the main component of the active material, as is the case for the nSi/RGO composite under investigation. Also silicon powder without any modification shows a high first discharge capacity but it also has the highest ICL. The large ICL is probably caused by SEI formation during the first lithiation due to higher crystallinity. Ball milled silicon shows a lower first discharge capacity, and lower ICL. This is most probably due to the fact that ball milled Si powders have more oxidized surfaces which act as a buffer of poor conductivity [44]. The large ICL exhibited by nSi/RGO can be ascribed both to the high surface of silicon nanoparticles and the absence of a surface passivation layer, probably removed during the high-temperature reduction step. The large exposed surface in the absence of a protective surface film gives rise to a great reactivity which results in a large ICL. Further irreversible capacity can be ascribed to Li storage at the surface, cavities and defects of the disordered carbon [45,46].

Below 0.15 V, a high and relatively broad peak shows up (A), corresponding to the sloping plateau in Fig. 4a at the same potential values. This feature can be associated with Li intercalation into the partly restacked RGO matrix and, mainly, to the first Si lithiation by Li. The latter process involves transformation of the pristine crystalline Si structure into amorphous Li_xSi alloys, with an expected final stoichiometry of $Li_{15}Si_4$ [35–47]. In the subsequent charge, and in the following cycles, two couples of reversible peaks are observed: (B), (C) at 0.3 V and 0.5 V during charge, and (D), (E) at 0.25 V and 0.05 V during discharge. These features can be respectively ascribed to reversible processes of Li–Si dealloying and alloying, respectively, occurring through formation of amorphous Li_xSi phases [13]. However, some low-potential irreversible features, related to Li–C storage and SEI formation, may still be observed during the discharges, evidencing that several cycles are needed to complete the irreversible processes.

The observed charge–discharge behavior is consistent with the one observed in Ref. [38], where the electrochemical response of a nSi/RGO active material prepared in similar conditions (but with different electrode and electrolyte formulations) had been analyzed. However, voltage values of the observed features are slightly shifted to lower values during discharge and to higher values during charge, probably related to the higher loading of the electrodes (4.6 vs. 1 mg/cm^2) that here induces higher cell polarization. For the same reason, the very low-potential peak usually associated with the formation of the crystalline $Li_{15}Si_4$ end-member [47] is not observed in the present case. The reduction of the cell performance due to the increase of the electrode load must be taken into consideration when designing electrochemical cells based on silicon anode in order to fully exploit the properties of this material. As regards the reversible capacity, it can be estimated from the values obtained during the charge steps (corresponding to Li release from the electrode), where there is no bias from irreversible processes. Upon electrode activation, the specific capacity values obtained during electrode charge progressively raise from 1040 mAh/g at first cycle to 1285 mAh/g at sixth cycle (normalized to the content of active Si). As noted earlier, charge and discharge capacities converge to the same value at sixth cycle, revealing that irreversible processes are no longer occurring. The low value of the specific capacity exhibited by silicon also argues in favor of the thesis that part of the irreversible capacity exhibited during the first discharge cycle can be related to lithium inserted into the silicon and which had become unavailable for subsequent cycles due to electric detachment of the silicon particles from the conductive RGO substrate.

To evaluate the effect of the charge current on the cell capacity, the cell was galvanostatically cycled at various currents equal to 0.15, 0.3, 0.75, 1.50, 3.00, and 7.50 mA (corresponding to a specific current range from approx. 170–7100 mA/g, normalized to the weight of Si). To ensure the same initial conditions, the cell was always discharged with a constant current of 0.15 mA. Considering the total capacity exhibited by the electrode in the last charge cycle (equal to 1.35 mAh), it

follows that the currents used to charge the electrode correspond to the rates of C/9, C/4.5 C/1.8, 1.1C, 2.2C, and 5.5C. The results of the test are shown in Fig. 5a and b. By increasing the charge current, the capacity decreases and the cell polarization increases. This trend is different from that observed in Ref. [40], where the capacity increased upon increase of the charge/discharge rate. This difference can be explained, once again, with the different loadings of the electrodes. In Ref. [40], the low electrode loading (about 1 mg/cm^2), together with the optimized electrode/electrolyte interface obtained by tailored formulations of the two systems, allowed a full utilization of the active material at every charge/discharge rate, so that the capacity and the efficiency were limited only by the mechanical stresses induced by the formation of the crystalline $Li_{15}Si_4$ end-member of the lithiation, more pronounced at low rates and negligible at higher rates. In the present case, the higher electrode loading (about 4.5×) induces an electrode polarization that results into the main limitation to active material utilization, and becomes more relevant as the current is increased. To establish the discharge performance of the nSi/RGO electrode at different current densities, the Peukert dependence is measured. The Peukert law is presented by Eq. (1) [48]:

$$C_r = T_{dis}I_{dis}{}^k \qquad (1)$$

where C_r represents the rated discharge capacity in mAh; and T_{dis} and I_{dis} are the discharge time and discharge current expressed in h and mA, respectively. The parameter k is the Peukert constant. The Peukert constant provides an indication of the power capability of the cell: the smaller the value of k, the higher the power capability. This parameter is strongly dependent on the battery technology: for lithium-ion technology, this parameter changes between 1.00 and 1.28 [49]. The effective capacity, C_e, is the product of the discharge time and discharge current. By rearranging Eq. (1), we can obtain Eq. (2) in which the effective capacity, C_e, is related to the rated discharge capacity C_r, Peukert constant k, and discharge current I_{dis}:

$$C_e = T_{dis}I_{dis} = C_rI_{dis}{}^{1-k} \qquad (2)$$

To evaluate the Peukert constant k, the specific discharge capacity is plotted as a function of the specific current in a double logarithmic plot as shown in Fig. 5b. From the slope of the curve, a Peukert constant k of 1.56 is calculated. The specific capacity extrapolated to zero current is about 3794 mAh/g if normalized to the Si content, and about 1286 mAh/g if normalized to the overall nSi/RGO composite active material, the latter value being quite close to the experimental charge/discharge capacity obtained in Ref. [40] with optimized electrode and electrolyte formulation.

3.3. Electrochemical characterization of the lithium-ion battery cell

The lithium cell containing the nSi/RGO-based electrode was opened and the electrode extracted. The electrode was used as an anode in a lithium-ion battery cell using a LiFePO$_4$-based electrode as a cathode. This strategy allowed to exploit the reversible capacity of the nSi/RGO anode avoiding the very high irreversible capacity loss needed for activation of the fresh electrode (see Par. 3.3). Despite commercial cells are generally limited by the cathode, in this experiment, we decided to prepare an anode limited cell for the exclusive purpose of obtaining information regarding the negative electrode. The cell was cycled at constant current of 0.08 mA (current density about 0.070 mA/cm^2) in charge and discharge. The charge was interrupted when 0.80 mAh of capacity was accumulated into the electrode. The discharge was interrupted when the cell voltage dropped off to 2.0 V. Fig. 6a shows the voltage profiles as a function of the specific capacity (based on the weight of nSi/RGO in the anode) for the above described cell. Fig. 6b reports the specific capacity, in charge and discharge. In the same figure, the Coulombic efficiency, defined as the ratio between the discharged
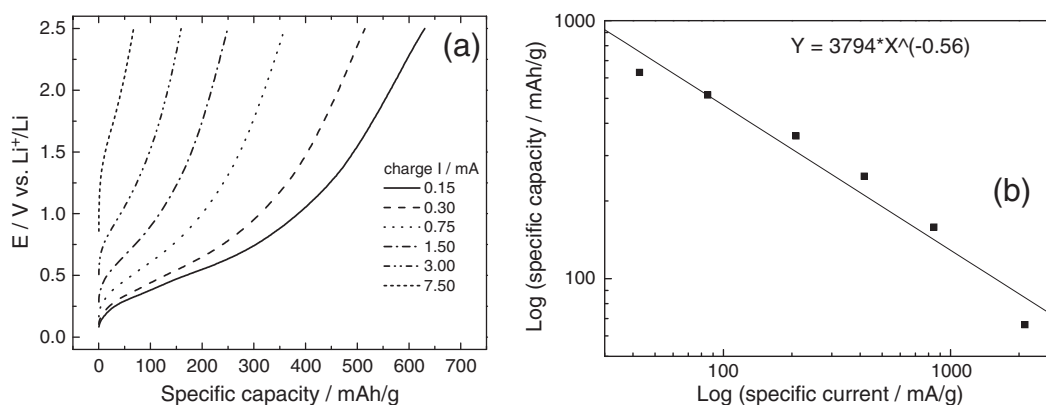
Fig. 5. (a) Voltage profiles as a function of the capacity for an electrode based on nSi/RGO evaluated at various charge currents. The charge currents are equal to 0.15, 0.3, 0.75, 1.50, 3.00, and 7.50 mA. The cell was discharged with a constant current of 0.15 mA. (b) Double logarithm plot showing the specific capacity as a function of the specific current.

capacity and the charge accumulated in the previous cycle, is also shown. The cell in the initial state has a voltage of about 1.8 V. During all the cycles the cell has charged for 10 hours accumulating the full allowed capacity (equal to 230 mAh/g). In the first discharge cycle, only the 50% of the charged capacity is released, probably due to a side reaction that consumes great part of the charged capacity. In subsequent cycles, the released capacity slowly tends to increase and, at the end of the test, the discharge capacity is increased up to 200 mAh/g. Unfortunately, the side reaction is not completely eliminated in the following cycles because the efficiency is always low and settles on 85%. The average discharge voltage was about 2.78 V. To evaluate the effect of the discharge current on the cell capacity, the lithium-ion cell was galvanostatically cycled at various discharge currents equal to 0.075, 0.150, 0.75, 1.5, 2.25, and 3.75 mA (current density values in the range 0.066–3.75 mA/ cm^2). The cell was always charged with a constant current of 0.075 mA, to ensure the same initial conditions. Considering the total capacity exhibited by the electrode active material in the last discharge cycle (equal to 0.68 mAh), it follows that the currents used to discharge the electrode correspond to the rates of C/9, C/4.5, 1.1C, 2.2C, 3.3C, and 5.5C. Fig. 7a shows the voltage profiles as a function of the specific capacity for a LiFePO$_4$/nSi–RGO lithium-ion battery cell cycled at the various discharge currents. When discharged at the lowest discharge current, the cell shows a high voltage plateau that extends for less than 0.2 mAh. Then the voltage monotonically decreases to reach the end discharge condition providing about 750 mAh/g. By increasing the discharge rate, the high voltage plateau, the capacity, and the average discharge voltage sharply decrease due to a severe polarization affecting the cell. By doubling the discharge current, a halving of the capacity is recorded. To evaluate the variation of the specific capacity at the various discharge rates, in Fig. 7b, the specific capacity values are

reported as a function of the specific current in a double logarithmic graph. Also in this case, a linear behavior is observed. The specific capacity extrapolated to zero current is about 3940 mAh/g while the value of the Peukert constant k is equal to 1.60. The similarity between these values and those found for the lithium cell shown in Fig. 5b allows to conclude that the battery performances are limited by the nSi/RGO-based electrode, namely, by the high polarization due to its thickness rather than by possible mechanical instability induced by Li$_{15}$Si$_4$ lithiation end-member, which formation is here prevented by the cell polarization.

4. Conclusions

The chemical–physical and electrochemical characterization of the nSi/RGO composite allowed to assess the characteristics of the material and its electrochemical behavior when used as an electrode in a lithium cell. It was found that the heat treatment under reducing atmosphere was effective in transforming the graphene oxide into graphene sheets. In agreement with the X-ray diffraction and scanning electron microscopy, it is possible to conclude that during this treatment, there has been a partial restacking of graphene sheets. The heat treatment did not affect the silicon that preserved a nanoscale morphology. The scanning electron micrograph revealed that, despite that Si nanoparticles and graphene nanosheets have undergone to a great mixing, the two phases are still easily distinguishable.

The thermal analysis allowed to estimate the amount of silicon present in the composite. The electrochemical characterization of the nSi/RGO composite performed in a lithium cell, carried out at low current, showed that the material presents a high first cycle irreversible capacity. In agreement with previous works, the irreversible capacity was
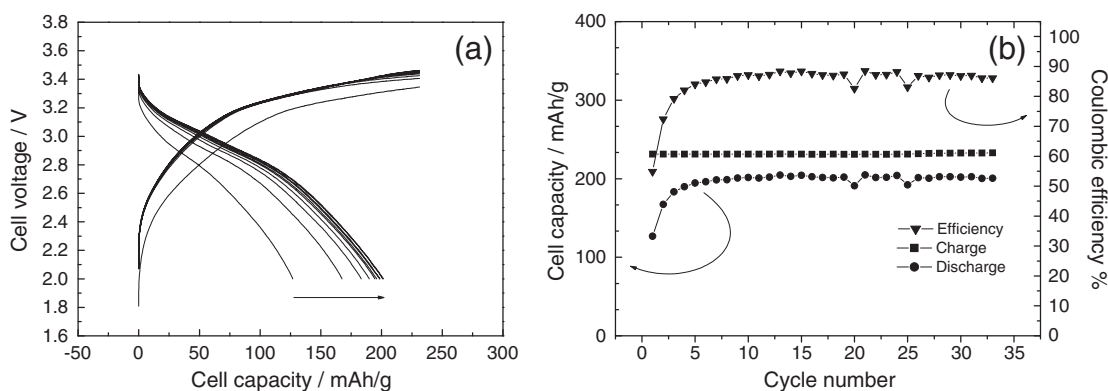

Fig. 6. (a) Voltage profiles as a function of the capacity for a LiFePO$_4$/nSi–RGO lithium-ion battery cell cycled at 0.08 mA. (b) Cell capacity as a function of the cycle number. Coulombic efficiency is also reported.
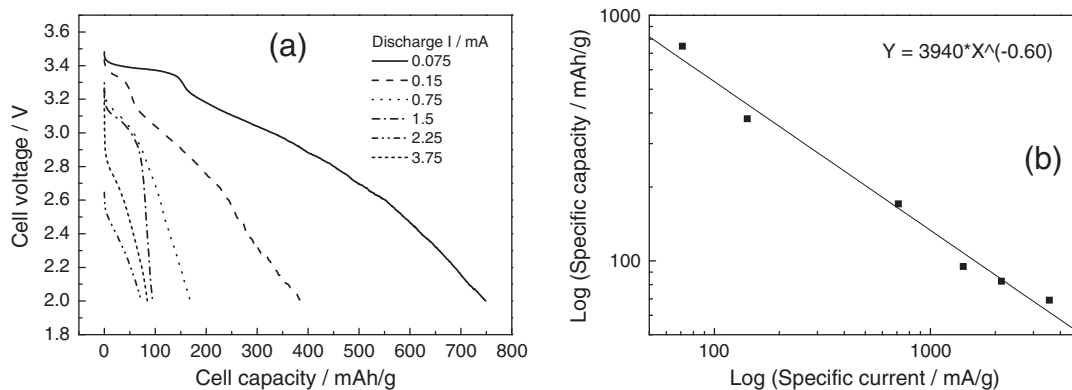
Fig. 7. (a) Voltage profiles as a function of the capacity for a LiFePO$_4$/nSi–RGO lithium-ion battery cell cycled at various discharge currents. The discharge currents are equal to 0.075, 0.150, 0.75, 1.5, 2.25, and 3.75 mA. The cell was charged with a constant current of 0.075 mA. (b) Double logarithm plot showing the specific capacity as a function of the specific current.

attributed to the formation of a passivation layer on the electrode surface or capture of lithium ions in cavities and defects present into the disordered carbon matrix. This irreversible reaction does not end at the first cycle as it continues even in the following cycles and it seems to be completed only after about six charge and discharge cycles. The electrode behavior is very sensitive to variations in current, and its capacity decreases, while the average charge voltage increases, with the increase of the charging current. The Peukert constant k was calculated to be 1.56. The electrode was used as an anode to assemble a full lithium-ion battery cell, by coupling the nSi/RGO electrode with a LiFePO$_4$-based cathode. Upon charge, the battery was capable of storing 230 mAh/g of capacity. In the first discharge, the battery released only 50% of the charged capacity. In subsequent cycles, the discharge capacity slowly increases. Nevertheless, the side reaction affecting the cell is not completely eliminated and the Coulombic efficiency at the last cycle was no higher than 0.85. When cycled at low discharge rate, the battery presents an average discharge voltage around 2.78 V and an anode active material specific capacity of about 750 mAh/g. By increasing the discharge rate, the capacity and the average discharge voltage sharply decrease. It was found that the doubling the discharge current determines a halving of capacity. The Peukert constant k was calculated to be 1.60. The similarity between the values of the Peukert constant allows to conclude that the performances of the battery are limited by the polarization of the 'thick' nSi/RGO-based anode.

References

[1] J.R. Szczech, S. Jin, Energy Environ. Sci. 4 (2011) 56–72.
[2] E. Radvanyi, E. De Vito, W. Porcher, J. Danet, P. Desbois, J.F. Colin, S.J.S. Larbi, J. Mater. Chem. A 1 (2013) 4956–4965.
[3] H. Jung, M. Park, Y.G. Yoon, G.B. Kim, S.K. Joo, J. Power Sources 115 (2003) 346–351.
[4] J.H. Ryu, J.W. Kim, Y.E. Sung, S.M. Oh, Electrochem. Solid-State Lett. 7 (2004) A306–A309.
[5] C.K. Chan, H.L. Peng, G. Liu, K. Mcilwrath, X.F. Zhang, R.A. Huggins, Y. Cui, Nat. Nanotechnol. 3 (2008) 31–35.
[6] M.H. Park, M.G. Kim, J. Joo, K. Kim, J. Kim, S. Ahn, Y. Cui, J. Cho, Nano Lett. 9 (2009) 3844–3847.
[7] H.C. Shin, J.A. Corno, J.L. Gole, M.L. Liu, J. Power Sources 139 (2005) 314–320.
[8] S. Cahen, R. Janot, L. Laffont-Dantras, J.M. Tarascon, J. Electrochem. Soc. 155 (2008) A512-A419.
[9] M. Holzapfel, H. Buqa, F. Krumeich, P. Novak, F.M. Petrat, C. Veit, Electrochem. Solid State Lett. 8 (2005) A516–A520.
[10] G. Wang, J. Yao, H. Liu, Electrochem. Solid-State Lett. 7 (2004) A250–A253.
[11] T. Cetinkaya, M. Guler, H. Akbulut, Microelectron. Eng. 108 (2013) 169–176.
[12] Z. Guo, E. Milin, J. Wang, J. Chen, H. Liu, J. Electrochem. Soc. 152 (2005) A2211–A2216.
[13] W. Wang, P.N. Kumta, ACS Nano 4 (2010) 2233–2241.
[14] A. Wilson, J. Dahn, J. Electrochem. Soc. 142 (1995) 326–332.
[15] S.J. Zhang, Y. Liang, Q. Zhou, Y. Peng, H. Yang, J. Power Sources 203 (2015) 976–982.
[16] S. Chew, Z. Guo, J. Wang, J. Chen, P. Munroe, S. Ng, L. Zhao, H. Liu, Electrochem. Commun. 9 (2007) 941–946.
[17] H. Kim, J. Cho, Nano Lett. 8 (2008) 3688–3691.
[18] J. Shu, H. Li, R. Yang, Y. Shi, X. Huang, Electrochem. Commun. 8 (2006) 51–54.
[19] S.L. Chou, J.Z. Wang, M. Choucair, H.K. Liu, J.A. Stride, S.X. Dou, Electrochem. Commun. 12 (2010) 303–306.
[20] R.Z. Hu, W. Sun, Y.L. Chen, M.Q. Zeng, M. Zhu, J. Mater. Chem. A 2 (2014) 9118–9125.
[21] C.L. Pang, H. Cui, G.W. Yang, C.X. Wang, Nano Lett. 13 (2013) 4708–4714.
[22] Y.J. Gong, S.B. Yang, L. Zhan, L.L. Ma, R. Vajtai, P.M. Ajayan, Adv. Funct. Mater. 24 (2014) 125–130.
[23] J.B. Chang, X.K. Huang, G.H. Zhou, S.M. Cui, P.B. Hallac, J.W. Jiang, P.T. Hurley, J.H. Chen, Adv. Mater. 26 (2014) 758–764.
[24] Y.Q. Zhang, X.H. Xia, X.L. Wang, Y.J. Mai, S.J. Shi, Y.Y. Tang, L. Li, J.P. Tu, Electrochem. Commun. 23 (2012) 17–20.
[25] M. Ko, S. Chae, S. Jeong, P. Oh, J. Cho, ACS Nano 8 (2014) 8591–8599.
[26] X.S. Zhou, Y.X. Yin, L.J. Wan, Y.G. Guo, Chem. Commun. 48 (2012) 2198–2200.
[27] B.P.N. Nguyen, N.A. Kumar, J. Gaubicher, F. Duclairoir, T. Brousse, O. Crosnier, L. Dubois, G. Bidan, D. Guyomard, B. Lestriez, Adv. Energy Mater. 3 (2013) 1351–1357.
[28] X. Zhao, C.M. Hayner, M.C. Kung, H.H. Kung, Adv. Energy Mater. 1 (2011) 1079–1084.
[29] K. Evanoff, A. Magasinski, J.B. Yang, G. Yushin, Adv. Energy Mater. 1 (2011) 495–498.
[30] N. Li, S.X. Jin, Q.Y. Liao, H. Cui, C.X. Wang, Nano Energy 5 (2014) 105–115.
[31] R. Yi, F. Dai, M.L. Gordin, H. Sohn, D. Wang, Adv. Energy Mater. 3 (2013) 1507–1515.
[32] R. Yi, F. Dai, M.L. Gordin, S. Chen, D. Wang, Adv. Energy Mater. 3 (2013) 295–300.
[33] W. Sun, R. Hu, H. Liu, M. Zeng, L. Yang, H. Wang, M. Zhu, J. Power Sources 268 (2014) 610–618.
[34] L. Ji, H. Zheng, A. Ismach, Z. Tan, S. Xun, E. Lin, V. Battaglia, V. Srinivasan, Y. Zhang, Nano Energy 1 (2012) 164–171.
[35] J.-G. Ren, Q.-H. Wu, G. Hong, W.-J. Zhang, H. Wu, K. Amine, J. Yang, S.-T. Lee, Energy Technol. 1 (2013) 77–84.
[36] K.S. Eom, T. Joshi, A. Bordes, I. Do, T.F. Fuller, J. Power Sources 249 (2014) 118–124.
[37] F. Maroni, R. Raccichini, A. Birrozzi, G. Carbonari, R. Tossici, F. Croce, R. Marassi, F. Nobili, J. Power Sources 269 (2014) 873–882.
[38] L.J. Cote, R. Cruz-Silva, J. Huang, J. Am. Chem. Soc. 131 (2009) 11027–11032.
[39] T. Nakajima, A. Mabuchi, R. Hagiwara, Carbon 26 (1988) 357–361.
[40] B.E. Deal, A.S. Grove, J. Appl. Phys. 36 (1965) 3770–3778.
[41] A. Birrozzi, R. Raccichini, F. Nobili, M. Marinaro, R. Tossici, R. Marassi, Electrochim. Acta 137 (2014) 228–234.
[42] I. Meschini, F. Nobili, M. Mancini, R. Marassi, R. Tossici, A. Savoini, M.L. Focarete, F. Croce, J. Power Sources 226 (2013) 241–248.
[43] F. Nobili, I. Meschini, M. Mancini, R. Tossici, R. Marassi, F. Croce, Electrochim. Acta 107 (2013) 85–92.
[44] C.-H. Yim, F.M. Courtelb, Y. Abu-Lebdeh, J. Mater. Chem. A 1 (2013) 8234–8243.
[45] N.A. Kaskhedikar, J. Maier, Adv. Mater. 21 (2009) 2664–2680.
[46] T. Zheng, W.R. McKinnon, J.R. Dahn, J. Electrochem. Soc. 143 (1996) 2137–2145.
[47] M.N. Obrovac, L. Christensen, Electrochem. Solid State Lett. 7 (2004) A93–A96.
[48] W. Peukert, Elektrotechnisch Z. 27 (1897) 287–288.
[49] N. Omar, P. Van den Bossche, T. Coosemans, J. Van Mierlo, Energies 6 (2013) 5625–5641.